Ceramics International 49 (2023) 13816–13822

Contents lists available at ScienceDirect

Ceramics International

journal homepage: www.elsevier.com/locate/ceramint

Ratiometric nanothermometer $CaSc_2O_4$: Nd^{3+} operating in biological window for deep-tissue photothermal therapy

Guotao Xiang [a,*], Menglin Yang [a], Yongxi Ding [a], Hongxiu Wu [a], Lu Yao [a], Yongjie Wang [a], Xianju Zhou [a], Li Li [a], Li Ma [c], Xiaojun Wang [c,**], Jiahua Zhang [b,***]

[a] Department of Mathematics and Physics, Chongqing University of Posts and Telecommunications, 2 Chongwen Road, Chongqing, 400065, China
[b] State Key Laboratory of Luminescence and Applications, Changchun Institute of Optics, Fine Mechanics and Physics, Chinese Academy of Sciences, 3888 Eastern South Lake Road, Changchun, 130033, China
[c] Department of Physics & Astronomy, Georgia Southern University, Statesboro, GA, 30460, USA

ARTICLE INFO

Handling Editor: Dr P. Vincenzini

Keywords:
Photothermal therapy
$CaSc_2O_4$: Nd^{3+}
Optical thermometry
Stark sublevel
Fluorescence intensity ratio

ABSTRACT

Accurate and real-time temperature detection is an urgent requirement in photothermal therapy (PTT). In this work, the $CaSc_2O_4$: Nd^{3+} nanorod with an average length of 150 nm has been determined to be an outstanding optical thermometer based on the fluorescence intensity ratio (*FIR*) of thermally coupled Stark sublevels of Nd^{3+}: $^4F_{3/2} \rightarrow {}^4I_{11/2}$ transition, of which the excitation and emission wavelength are located in the first and second biological window respectively, resulting in an 8 mm penetration depth in the biological tissues. The maximal absolute sensitivity and relative sensitivity as well as the minimal temperature resolution of the present sample is 0.0008 K^{-1}, 0.0018 K^{-1} and 0.19 *K* respectively, which is superior to the vast majority of the same type thermometers. Besides that, the nanorods show a 7 *K* temperature increment after 180 s' 808 nm-laser radiation, revealing its photothermal conversion capacity thanks to the considerable nonradiative relaxation processes among the metastable energy levels of Nd^{3+}. These results indicate that Nd^{3+} single-doped $CaSc_2O_4$ nanorods can be utilized as the optical thermometer in the deep-tissue PTT process for real-time thermometry along with the function of light-to-heat conversion.

1. Introduction

Nowadays, human health has been more and more widely concerned with the development of science and technology. A series of novel effective technologies have been proposed of cancer therapy, such as photodynamic therapy, drug delivery and photothermal therapy (PTT), etc. [1-3] Thereinto, PTT is regarded as one of the most promising method for tumor treatment with minimally invasive and minor side effects, which kills cancer cells through converting photon energy into heat. However, the normal cells can also be destroyed by excessive temperature during the PTT process [4-6]. Therefore, the therapy temperature of PPT should be precisely monitored in real time to not only damage the diseased cells, but also ensure the normal cell survival.

Lanthanide ion doped upconversion (UC) nano materials have be demonstrated to own the advantages of short response time, large spatial resolution, high accuracy, non-contact and strong electromagnetic interference resistance for optical temperature detection in vivo [7-13]. Meanwhile, the current studies involved with UC optical thermometry are mainly focused on Yb^{3+}/Er^{3+} codoped system, of which the thermometric behavior is realized by the fluorescence intensity ratio (*FIR*) of thermally coupled green levels Er^{3+}: $^2H_{11/2}/{}^4S_{3/2}$ under the excitation of 980 nm wavelength [14-16]. However, the 980 nm-laser-induced heating effect as well as the shallow penetration depth of green light in the biological tissues severely restricts the practical application of Yb^{3+}/Er^{3+}-based thermometers [17-19]. It is an urgent need to develop a novel optical thermometer with the excitation and emission wavelength simultaneously locating in biological window (BW), including I-BW (700 nm–950 nm), II-BW (1000 nm–1400 nm) and so on.

Nd^{3+} single-doped luminescent materials may be an ideal candidate to fit the above requirements due to its inherent property of emitting near infrared (NIR) light situated in II-BW under the excitation of 808

* Corresponding author.
** Corresponding author.
*** Corresponding author.
E-mail addresses: xianggt@cqupt.edu.cn (G. Xiang), xwang@georgiasouthern.edu (X. Wang), zhangjh@ciomp.ac.cn (J. Zhang).

https://doi.org/10.1016/j.ceramint.2022.12.260
Received 6 October 2022; Received in revised form 23 December 2022; Accepted 27 December 2022
Available online 28 December 2022

nm wavelength (locating in I-BW), which is beneficial for eliminating the laser-induced heating effect and improving the penetration depth [20-22]. Moreover, Nd^{3+} ion can also be employed as NIR light-to-heat converter by virtue of a series of nonradiative relaxation (NR) processes among its abundant metastable energy levels with small energy gap (ΔE). That is to say, temperature sensing operating in BW region along with photothermal conversion ability can be anticipated to simultaneously accomplish in Nd^{3+} single-doped system [23-33].

Herein, Nd^{3+} single-doped $CaSc_2O_4$ nanorods are successfully prepared by the hydrothermal method, which shows excellent temperature sensing performance based on the *FIR* of the thermally coupled Stark sublevels of Nd^{3+}: $^4F_{3/2} \rightarrow {}^4I_{11/2}$ transition. Moreover, the detection depth of the present nanorods can reach an 8-mm-thickness in the biological tissues, benefiting from the location of its excitation and emission wavelength in the BW region. Beyond that, the photothermal conversion ability is also found in the Nd^{3+} single-doped nanorods. All the results reveal that the $CaSc_2O_4$: Nd^{3+} nanorod is a promising material for temperature sensing during the deep-tissue PTT process along with light-to-heat conversion capacity.

2. Experimental

2.1. Chemicals

$CaCO_3$ and HNO_3 are supplied by Aladdin. NaOH and ethanol are supplied by Chongqing Chuandong Chemical (Group) Co. Ltd. Sc_2O_3 (99.99%) and Nd_2O_3 (99.99%) are supplied by Sinopharm Chemical Reagent Company of China. All the reagents are used as raw materials without further purification.

2.2. Synthesis of $CaSc_2O_4$: x% Nd^{3+} (x = 0.5, 1, 1.5, 2, 2.5)

$CaCO_3$, Sc_2O_3 and Nd_2O_3 were initially dissolved in HNO_3 under the stirring condition for 3 h to form a homogeneous nitrate solution. Then, NaOH was added into the above solution to adjust its pH value to 12. After that, the solution was transferred into a 50 ml Teflon-lined autoclave and maintained at 190 °C for 10 h, then naturally cooled to room temperature. The products were washed with distilled water and absolute ethanol in turn. Finally, the samples were dried in the oven and annealed at 700 °C for 3 h.

2.3. Characterization

Powder X-ray diffraction (XRD) data are collected by a Persee XD-2 diffractometer. The morphology is performed by a JEOL JEM 2100 transmission electron microscopy (TEM). A FLS1000 spectrometer supplied by Edinburgh Instruments equipped with an 808 nm laser as the excitation source is employed to measure the spectroscopic data. A Linkam HFS600E-PB2 temperature controlling equipment cooperated with the FLS1000 spectrometer mentioned above is used to measure the temperature dependent luminescence spectra. The lifetime values are calculated by integrating the area of the corresponding normalized decay curves.

3. Results and discussion

3.1. Structure

Fig. 1(a) illustrates the XRD patterns of $CaSc_2O_4$ doped with various Nd^{3+} concentration. Evidently, the positions and relative intensities of the diffraction peaks for every sample match well with the standard XRD data of $CaSc_2O_4$ (PDF#20–0234), revealing that Nd^{3+} ions (ionic radius 0.995 Å) have been successfully doped into $CaSc_2O_4$ matrix to form a solid solution structure by occupying the Ca^{2+} ion (ionic radius 0.99 Å) sites due to their close ionic radius, according to the previous reports [34]. As shown in Fig. 1(b), the size and morphology properties of $CaSc_2O_4$: 1% Nd^{3+} are investigated by TEM technology, in which the sample exhibits a nanorod morphology with an average length of 150 nm and diameter of 40 nm. The length distribution of $CaSc_2O_4$: 1% Nd^{3+} nanorods is presented in Fig. S1. Well-resolved lattice fringes with interplanar spacing of 2.72 Å are clearly observed in the high-resolution TEM (HR-TEM) image of $CaSc_2O_4$: 1% Nd^{3+} (see Fig. 2(c)), corresponding to (320) crystal planes of orthorhombic phase $CaSc_2O_4$ (PDF#20–0234), further demonstrating the successful construction of $CaSc_2O_4$: Nd^{3+} nanorods.

3.2. Luminescence properties

Fig. 2(a) presents the photoluminescence (PL) spectra of Nd^{3+}: $^4F_{3/2} \rightarrow {}^4I_{11/2}$ transition in $CaSc_2O_4$: x% Nd^{3+} (x = 0.5, 1, 1.5, 2, 2.5) nanorods, which are measured under the same test conditions. Obviously, four narrow peaks are included in the emission band, located at 1065 nm, 1076 nm, 1087 nm and 1102 nm respectively, which are derived

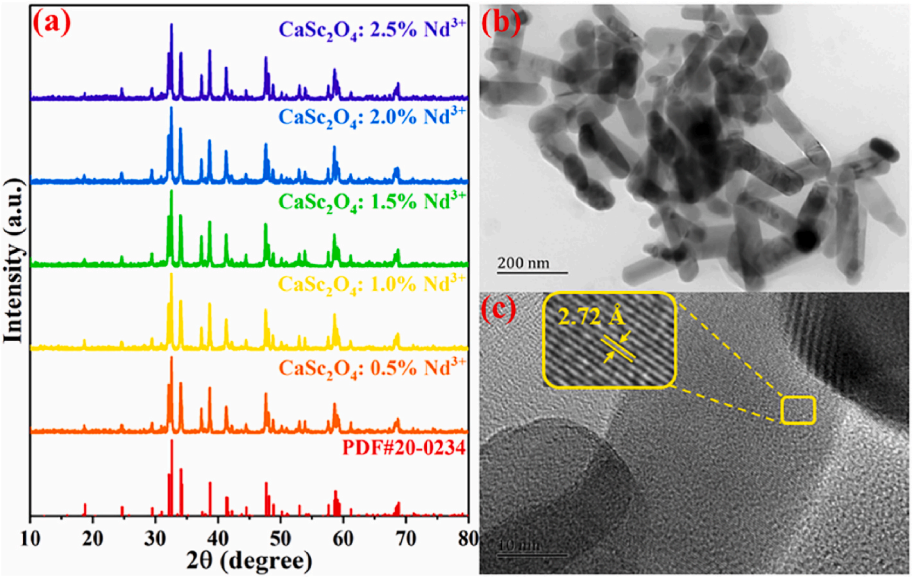

Fig. 1. (a) The XRD patterns of $CaSc_2O_4$: x% Nd^{3+} (x = 0.5, 1, 1.5, 2, 2.5). (b) The TEM image of $CaSc_2O_4$: 1% Nd^{3+}. (c) The HR-TEM image of $CaSc_2O_4$: 1% Nd^{3+}.

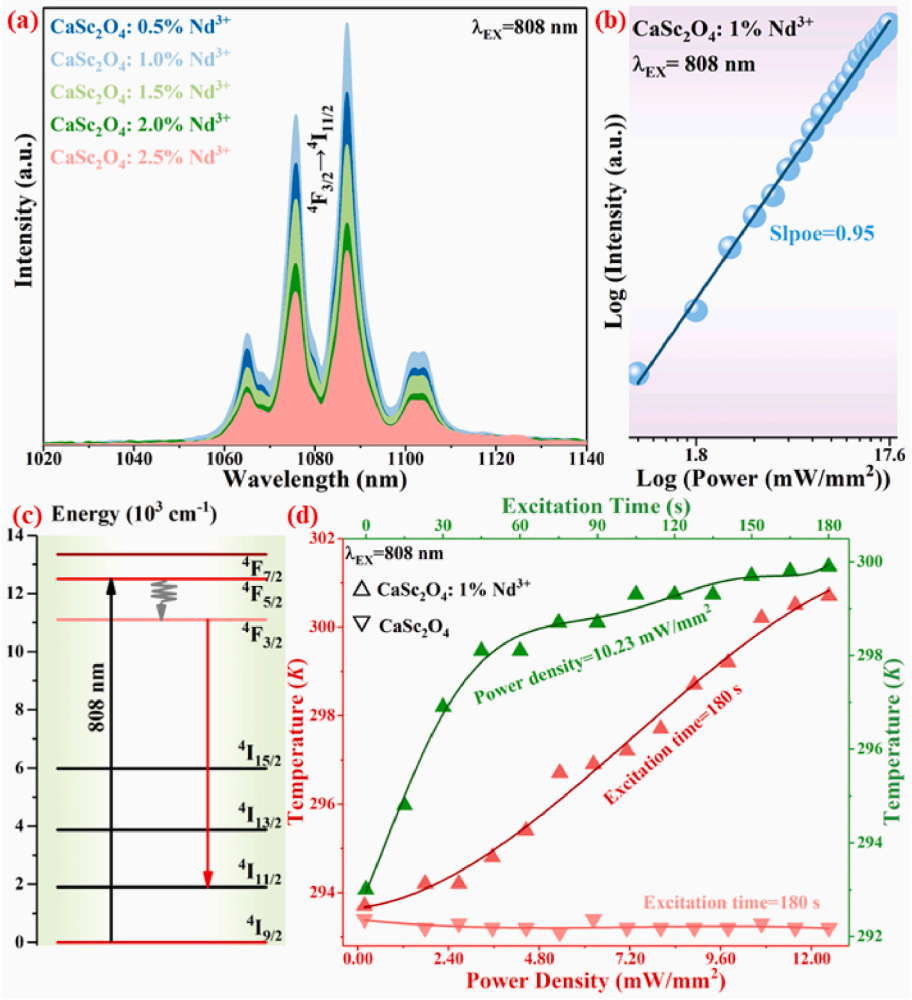

Fig. 2. (a) Emission spectra of $CaSc_2O_4$: x% Nd^{3+} (x = 0.5, 1, 1.5, 2, 2.5) nanorods. (b) The log(*I*) - log(*P*) diagram of Nd^{3+}: $^4F_{3/2} \rightarrow {}^4I_{11/2}$ transition in $CaSc_2O_4$: 1% Nd^{3+}. (c) The energy level diagram of Nd^{3+} excited by 808 nm wavelength. (d) The photothermal conversion effect of Nd^{3+}-free $CaSc_2O_4$ and $CaSc_2O_4$: 1% Nd^{3+} nanorods radiated by 808 nm wavelength.

from the Stark splitting of $^4F_{3/2}$ and $^4I_{11/2}$ energy level. Meanwhile, it can be definitely determined that the optimal doping concentration of Nd^{3+} is 1%, through which the strongest $^4F_{3/2} \rightarrow {}^4I_{11/2}$ transition can be obtained. When the doping concentration of Nd^{3+} exceeds this optimal value, the NIR emission intensity would be rapidly weakened due to the serious cross relaxation (CR) processes among Nd^{3+} ions. In addition, the excitation power density dependence of Nd^{3+}: $^4F_{3/2} \rightarrow {}^4I_{11/2}$ transition is investigated to clarify the transition mechanism of Nd^{3+} single-doped $CaSc_2O_4$ excited by 808 nm wavelength. The relationship between intensity *I* and excitation power density *P* can be represented as follows:

$$I \propto P^n \tag{1}$$

Here *n* represents the required number of photons for populating one activator from the ground state to the corresponding excited level, which can be obtained by the slope of the linear curve of log(*I*) and log (*P*). As depicted in Fig. 2(b), the *n* value is calculated to be approximately 1.0, revealing a single photon process for Nd^{3+}: $^4F_{3/2} \rightarrow {}^4I_{11/2}$ transition.

As shown in Fig. 2(c), under the excitation of 808 nm wavelength, the Nd^{3+} at the ground state can be directly pumped to $^4F_{5/2}$ level and then de-excited down to $^4F_{3/2}$ level through a NR process. Subsequently, the Nd^{3+} at $^4F_{3/2}$ level can radiatively transfer to the lower energy states, including $^4I_{9/2}$, $^4I_{11/2}$, $^4I_{13/2}$ and $^4I_{15/2}$. It should be noted that the de-excitation of the above energy levels to the ground state are mainly realized by NR processes, resulting in the generation of photothermal conversion effect. Therefore, in order to evaluate the light-to-heat conversion ability of the present nanorods, the temperature of $CaSc_2O_4$: 1% Nd^{3+} powder sample are real-time detected by an infrared thermometer under the excitation of 808 nm wavelength. As plotted in Fig. 2(d), the sample temperature (293 *K*) is gradually raised with the radiation time extension and comes up to equilibrium temperature 300 *K* after about 180 s. Meanwhile, when the exposure time of the sample is fixed at 180 s, its temperature is also increased distinctly with the enhancement of excitation power, giving rise to a 7 *K* increment. In addition, no obvious temperature variation is found in Nd^{3+}-free $CaSc_2O_4$ nanorods, demonstrating that the excitation light has no heating effect for $CaSc_2O_4$ matrix and the light-to-heat conversion ability of $CaSc_2O_4$: 1% Nd^{3+} nanorods is mainly attributed to the absorption of Nd^{3+} for 808 nm laser followed by a sequence of NR processes.

3.3. Temperature sensing properties

The PL spectra of $CaSc_2O_4$: 1% Nd^{3+} nanorods as a function of temperature are measured under the excitation of 808 nm wavelength, as shown in Fig. 3(a) and Fig. S2. Notably, the NIR emission band emerges a few differences with the growth of temperature. On the one hand, the spectral positions of the emission lines are found to undergo a thermal red shift along with temperature increase, influenced by the electron-phonon coupling effect. Specifically, the local environment of

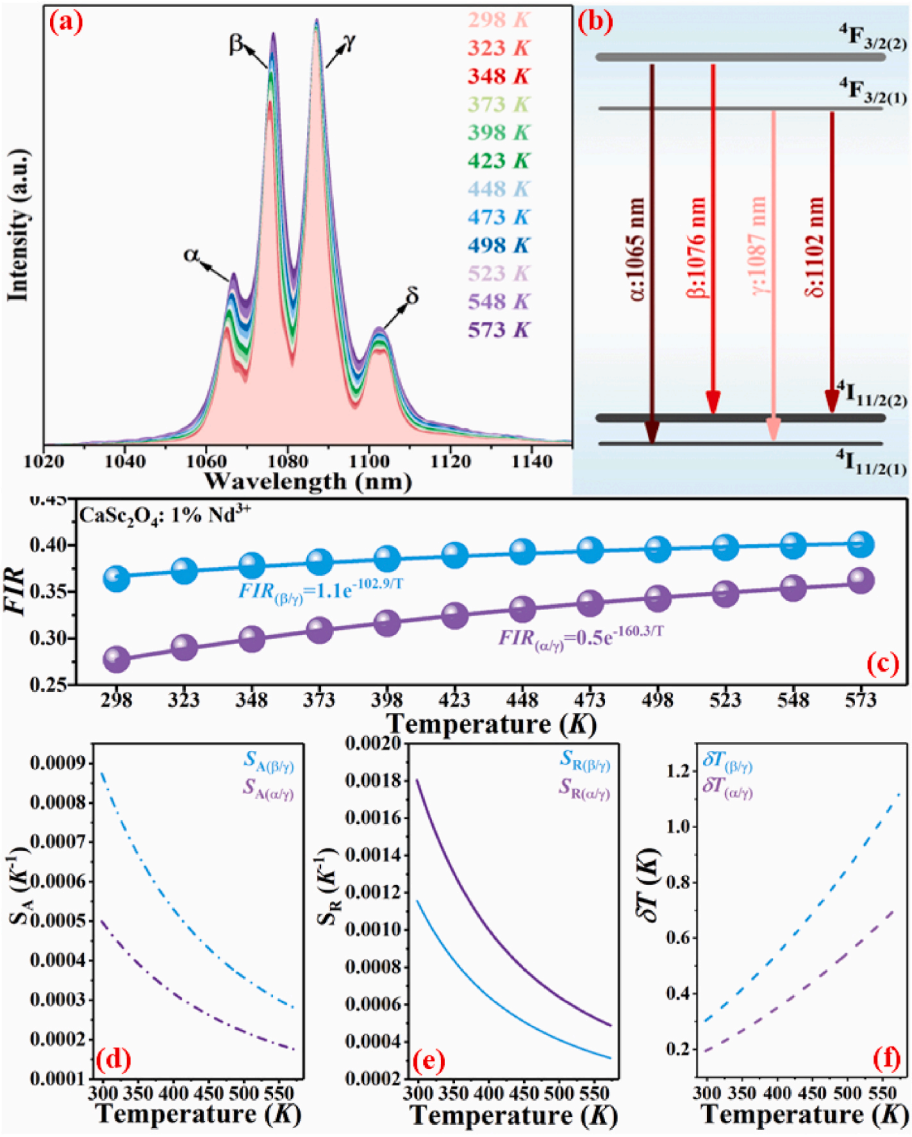

Fig. 3. (a) Temperature-dependent PL spectra of $CaSc_2O_4$: 1% Nd^{3+} nanorods normalized at 1087 nm. (b) An equivalent four-level system for depicting Nd^{3+}: $^4F_{3/2}$ → $^4I_{11/2}$ transition. The (c) *FIR*, (d) absolution sensitivity S_A, (e) relative sensitivity S_R and (f) temperature resolution δT as a function of temperature in $CaSc_2O_4$: 1% Nd^{3+} nanorods.

Nd^{3+} ions is randomly perturbed by host vibration modes at high temperature, which causes the energy loss of the emitted phonons and then a slight shift of each Stark transition toward long wavelength (low energy) direction occurs. On the other hand, although the whole emission intensity of Nd^{3+}: $^4F_{3/2}$ → $^4I_{11/2}$ transition decreases with the rising temperature due to the so-called temperature quenching, the relative emission intensities of the Stark transitions change regularly with the increase of temperature, attributed to the fact of thermal coupling property among the Stark sublevels, which makes it possible for optical thermometry.

Here, in order to better study the thermal properties of the Stark sublevels of Nd^{3+}: $^4F_{3/2}$ → $^4I_{11/2}$ transition, an equivalent four-level system is proposed, as visualized in Fig. 3(b). In this system, both $^4F_{3/2}$ and $^4I_{11/2}$ multiplets are regarded as a two-level system, consisting of a lowest Stark sublevel and a group of higher Stark sublevels respectively. More specifically, the remaining Stark components are regarded as a whole except for the lowest Stark sublevel. In this case, the strongest emission peak located at 1087 nm should be ascribed to the transition from the lowest Stark sublevel of $^4F_{3/2}$ to the lowest Stark sublevel of $^4I_{11/2}$ according to the Boltzmann distribution law, namely γ: $^4F_{3/2(1)}$ → $^4I_{11/2(1)}$. Sequentially, with the increasing of temperature, it can be seen that the Stark transitions at 1065 nm and 1076 nm are more obviously enhanced relative to the transition γ, manifesting that both of them originate from the upper Stark sublevel $^4F_{3/2(2)}$, namely α: $^4F_{3/2(2)}$ → $^4I_{11/2(1)}$ and β: $^4F_{3/2(2)}$ → $^4I_{11/2(2)}$ respectively. Then, the location of transition δ: $^4F_{3/2(1)}$ → $^4I_{11/2(2)}$ can be calculated by the following equation:

$$|E_\alpha - E_\gamma| = |E_\beta - E_\delta| \quad (2)$$

Here E is the activation energy of the corresponding level [35]. According to the above calculation, the emission wavelength of transition δ is determined to be 1098 nm, closed to the experimental value 1102 nm as shown in Fig. 3(a), indicating the reliability of the proposed equivalent four-level system.

Considering the small ΔE between $^4F_{3/2(1)}$ and $^4F_{3/2(2)}$, the two Stark sublevels should be thermally coupled and their *FIR* should comply with the Boltzmann distribution law:

$$FIR_{(\alpha/\gamma)} = I_\alpha/I_\gamma = B_1 \cdot exp(-\Delta E_1/K_B T), \quad (3)$$

$$FIR_{(\beta/\gamma)} = I_\beta/I_\gamma = B_2 \cdot exp(-\Delta E_2/K_B T). \quad (4)$$

where I, K_B and T represent the luminescence intensity, Boltzmann constant and absolute temperature, respectively [36-41]. Sequentially, the NIR emission band of Nd^{3+}: $^4F_{3/2} \rightarrow {}^4I_{11/2}$ transition is fitted by four Gaussian functions as visualized in Fig. S3, which are used to acquire the corresponding integrated intensity of each Stark transitions. In this way, the temperature calibration curves based on *FIR* values are fitted by using the above functions, as shown in Fig. 3(c). Utilizing the calibration curves, the values of ΔE_1 and ΔE_2 are calculated to be 111.51 cm^{-1} and 71.51 cm^{-1} respectively, deviating from their corresponding values obtained from the emission spectra (190.03 cm^{-1} of ΔE_1 and 94.05 cm^{-1} of ΔE_2) due to the enhancement of the multi-phonon relaxation processes at high temperature [42].

To compare the temperature sensing performances of the present sample with others, the key parameters, absolute sensitivity S_A and relative sensitivity S_R, are worked out by the following equations:

$$S_A = |d(FIR)/dT| = FIR \cdot \Delta E/(K_B \cdot T^2), \quad (5)$$

$$S_R = |d(FIR)/(FIR) \cdot dT| = \Delta E/(K_B \cdot T^2). \quad (6)$$

As plotted in Fig. 3(d) and (e), the S_A and S_R of both $FIR_{(\alpha/\gamma)}$ and $FIR_{(\beta/\gamma)}$ are monotonously decreased with the rising temperature and reached their corresponding maximum value 0.0005 K^{-1} of $S_{A(\alpha/\gamma)}$, 0.0008 K^{-1} of $S_{A(\beta/\gamma)}$, 0.0018 K^{-1} of $S_{R(\alpha/\gamma)}$ and 0.0011 K^{-1} of $S_{R(\beta/\gamma)}$ at the initial temperature. As can be seen from Table 1, the $CaSc_2O_4$: Nd^{3+} nanorods exhibit larger sensitivity than majority of the other Nd^{3+}-based optical temperature sensors reported previously, indicating its excellent optical thermometry ability. More importantly, the optimal working zone of the present nanorods just locate in the range of physiological temperature, which makes it a certain potential application for temperature sensing in vivo.

Another pivotal parameter of the luminescent thermometers is the temperature resolution δT, namely temperature uncertainty, can be obtained by the following equation [50]:

$$\delta T = (\delta FIR/FIR) \cdot (1/S_R). \quad (7)$$

Here $\delta FIR/FIR$ is the relative uncertainty of *FIR*, mainly related to the equipment. In our case, the $\delta FIR/FIR$ value is about 0.035% for the equipment we used for spectrum measurement, which is obtained by consecutively collecting the emission spectra of $CaSc_2O_4$: 1% Nd^{3+} nanorods for 50 times. As illustrated in Fig. 3(f), the curves of both $\delta T_{(\alpha/\gamma)}$ and $\delta T_{(\beta/\gamma)}$ possess the minimal value of 0.19 *K* and 0.30 *K* at 298 *K* respectively and then increase with the rising temperature.

Next, a proving experiment is designed and conducted to explore the practicality of the present sample for temperature sensing based on *FIR* technology. Firstly, the sample is heated to a certain temperature by a heating gun. Then, the surface and inner temperature of the sample are detected by an infrared thermometer and the *FIR* technology, respectively. As shown in Fig. 4, both the surface and inner temperature are almost linearly raised under the ongoing heating process, but a distinct temperature deviation between them is also found, which is ascribed to heat loss during its diffusion process from the sample surface to interior.

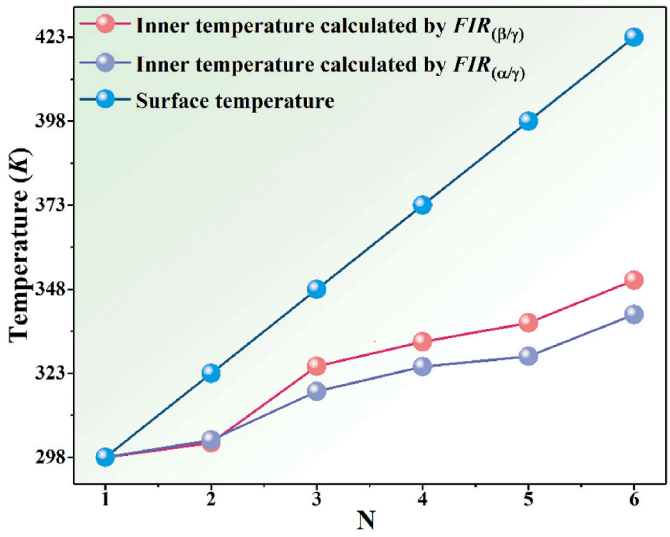

Fig. 4. The sample temperature determined by $FIR_{(\alpha/\gamma)}$ and $FIR_{(\beta/\gamma)}$ as well as the infrared thermometer. N is the testing order during the proving experiment.

Fortunately, the inner temperature calculated by $FIR_{(\alpha/\gamma)}$ is very similar as that obtained by $FIR_{(\beta/\gamma)}$, verifying the excellent temperature sensing performance of the present nanorods. Besides that, the $FIR_{(\alpha/\gamma)}$ and $FIR_{(\beta/\gamma)}$ values keep almost unchanged after conducting five cycling processes, revealing their outstanding repeatability for temperature sensing, as depicted in Fig. S4.

In addition, the temperature dependence of lifetime τ of Nd^{3+}: $^4F_{3/2}$ level is investigated and illustrated in Fig. S5. Notably, the lifetime is gradually decreased from 152 μs to 123 μs with the increasing temperature due to the enhancement of NR processes [51]. More importantly, an linear relationship exists between the lifetime values of Nd^{3+}: $^4F_{3/2}$ level and the temperature, as shown in Fig. 5, which means a new way for $CaSc_2O_4$: Nd^{3+} nanorods to detect the temperature. In this case, the S_A curve shows a horizontal straight line with an unchanged value of 0.0001 K^{-1} and the S_R curve is increased with the rising temperature and reached its maximum value 0.00082 K^{-1} at 573 *K*.

3.4. Ex vivo experiments in biological tissues

As we all know, penetration depth in the biological tissues is an extremely important parameter for PTT agents. Therefore, the detection depth of the NIR emission of $CaSc_2O_4$: 1% Nd^{3+} nanorods in the biological tissues is evaluated by a straightforward *ex vivo* experiment, in which the NIR spectra of the present sample are collected by an FLS1000 spectrometer at different biological tissue thickness under the room temperature. As depicted in Fig. 6 and Fig. S6, the PL intensity is dramatically reduced with the increasing tissue thickness. Nevertheless, no obvious variation is found in the NIR spectral profile with the

Table 1
Various Nd^{3+}-based optical thermometers with related parameters.

Materials	Dopant	EX	Wavelength (nm)	Temperature (*K*)	S_R (K^{-1})	S_A (K^{-1})	Ref.
$CaSc_2O_4$	Nd^{3+}	808 nm	1020–1140	298–573	0.0018	0.0008	This work
$Y_3Al_5O_{12}$	Nd^{3+}	808 nm	935–950	283–343	0.0015	~0.0012	[43]
LaF_3	Nd^{3+}	808 nm	900–1060	283–333	0.0010	~0.0005	[44]
CaF_2	Nd^{3+}	808 nm	980–1200	295–335	0.0012	~0.0002	[45]
	Nd^{3+}/Y^{3+}	808 nm	980–1200	295–335	0.0016	~0.0001	[45]
$NaYF_4$	Nd^{3+}	830 nm	860–900	273–423	0.0012	~0.0006	[46]
$Gd_3Sc_2Al_3O_{12}$	Nd^{3+}	806 nm	930–960	293–323	0.0016	–	[47]
$KLaP_4O_{12}$	Nd^{3+}	830 nm	840–930	83–600	0.0009	–	[48]
$NaLaP_4O_{12}$	Nd^{3+}	830 nm	840–930	83–600	0.0010	–	[48]
$RbLaP_4O_{12}$	Nd^{3+}	830 nm	840–930	83–600	0.0010	–	[48]
YVO_4	Nd^{3+}	808 nm	1055–1075	123–398	0.0047	–	[49]

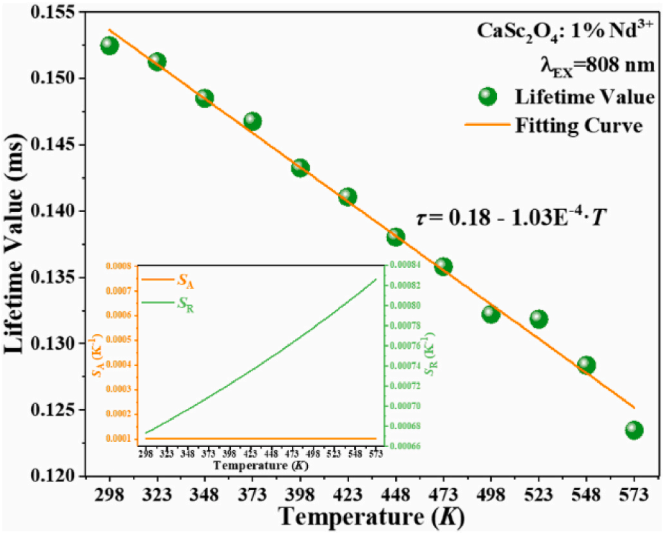

Fig. 5. Fitting curve of lifetime values of Nd^{3+}: $^4F_{3/2}$ level as a function of temperature along with the corresponding S_A and S_R in the inset.

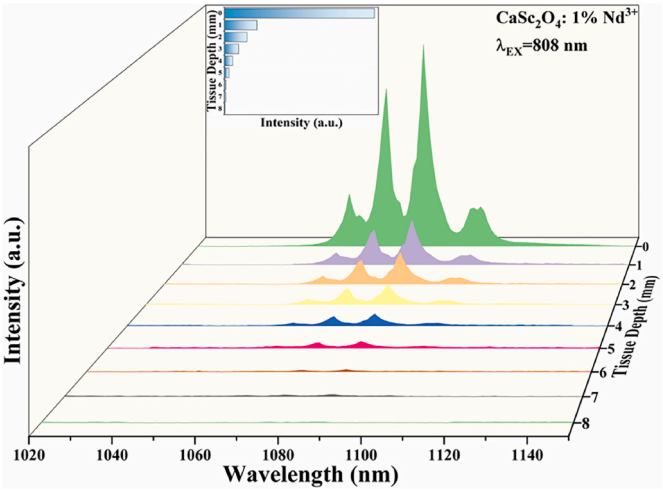

Fig. 6. The NIR emission spectra of $CaSc_2O_4$: 1% Nd^{3+} nanorods with various biological tissue thickness.

increase of biological tissue thickness. Moreover, the NIR luminescence can still be captured by the spectrum equipment until the biological tissues reach 8-mm-thickness because of the negligible absorption and scattering effect of the biological tissues in II-BW, implying its potential for utilization in the deep tissues.

4. Conclusions

In conclusion, a novel optical thermometer $CaSc_2O_4$: Nd^{3+} nanorods operating in the BW has been successfully synthesized by a hydrothermal method. Under the excitation of 808 nm wavelength, the strong Nd^{3+}: $^4F_{3/2} \rightarrow {}^4I_{11/2}$ transition locating in II-BW region can be obtained, consisting of four dominating Stark splitting. Then, the temperature sensing behavior is realized by the *FIR* of these thermally coupled Stark sublevels with the maximal S_A and S_R of 0.0008 K^{-1} and 0.0018 K^{-1} as well as the minimal δT of 0.19 *K*, which is superior to the vast majority of the same type thermometers. Meanwhile, the lifetime values of Nd^{3+}: $^4F_{3/2}$ level also exhibit excellent optical thermometry performance with maximum S_R of 0.00082 K^{-1}. In addition, the present sample shows photothermal conversion capacity under the excitation of 808 nm wavelength, from which a 7 *K* temperature increment can be obtained after 180 s' exposure time. The penetration depth of the NIR light originating from Nd^{3+}: $^4F_{3/2} \rightarrow {}^4I_{11/2}$ transition is examined to be 8 mm by a simple *ex vivo* experiment. These data indicate that $CaSc_2O_4$: Nd^{3+} is a promising nano-thermometer with the ability of light-to-heat conversion and can be used for real time temperature measurement in deep-tissue PTT process.

Declaration of competing interest

The authors declare that they have no known competing financial interests or personal relationships that could have appeared to influence the work reported in this paper.

Acknowledgements

This work is financially supported by National Natural Science Foundation of China (11704054, 11874055, 12004062, 52104392) and Science and Technology Research Program of Chongqing Municipal Education Commission (KJZD-K201800602, KJZD-M202000601, KJQN202100615, KJQN202100639).

Appendix A. Supplementary data

Supplementary data to this article can be found online at https://doi.org/10.1016/j.ceramint.2022.12.260.

References

[1] D. Stdab, X. Yao, W. Xi, B. Artur, R. Wei, S. Lining, Nd^{3+}-sensitized upconversion nanoparticle coated with antimony shell for bioimaging and photothermal therapy invitro using single laser irradiation, J. Rare Earths 40 (2021) 862–869, https://doi.org/10.1016/j.jre.2021.05.015.

[2] Y. Xing, L. Li, X. Ai, L. Fu, Polyaniline-coated upconversion nanoparticles with upconverting luminescent and photothermal conversion properties for photothermal cancer therapy, Int. J. Nanomed. 11 (2016) 4327, https://doi.org/10.2147/IJN.S97441.

[3] Su, Y. Zhao, Y. Huang, Y. Lian, S. Xu, G. Bai, Bi-functional nanocomposite based on phosphor and carbon nanotubes for tumor ablation in a photothermal fiber system with temperature feedback, Chem. Eng. J. 436 (2022), 134994, https://doi.org/10.1016/j.cej.2022.134994.

[4] F. Fani, E. Schena, P. Saccomandi, S. Silvestri, CT-based thermometry: an overview, Int. J. Hyperther. 30 (2014) 219–227, https://doi.org/10.3109/02656736.2014.922221.

[5] Y. Wang, W. Du, T. Zhang, Y. Zhu, Y. Ni, C. Wang, F. Raya, L. Zou, L. Wang, G. Liang, A self-evaluating photothermal therapeutic nanoparticle, ACS Nano 14 (2020) 9585–9593, https://doi.org/10.1021/acsnano.9b10144.

[6] D. Jaque, L.M. Maestro, B.D. Rosal, P. Haro-Gonzalez, A. Benayas, J.L. Plaza, M. E. Rodrıguez, J.G. Sole, Nanoparticles for photothermal therapies, Nanoscale 6 (2014) 9494–9530, https://doi.org/10.1039/C4NR00708E.

[7] X. Wang, Q. Liu, Y. Bu, C. Liu, T. Liu, X. Yan, Optical temperature sensing of rare-earth ion doped phosphors, RSC Adv. 5 (2015) 86219–86236, https://doi.org/10.1039/C5RA16986K.

[8] F. Vetrone, R. Naccache, A. Zamarrón, D. Juarranz, F. Sanz-Rodriguez, M. L. Martinez, R.E. Martin, D. Jaque, S.J. Garcla, J. Capobianco, Temperature sensing using fluorescent nanothermometers, ACS Nano 4 (2010) 3254–3258, https://doi.org/10.1021/nn100244a.

[9] A.A. Ansari, A.K. Parchur, M.K. Nazeeruddin, M.M. Tavakoli, Luminescent lanthanide nanocomposites in thermometry: chemistry of dopant ions and host matrices, Coord. Chem. Rev. 444 (2021), 214040, https://doi.org/10.1016/j.ccr.2021.214040.

[10] X. Liu, T. Li, X. Zhao, H. Suo, Z. Zhang, P. Zhao, S. Gao, M. Niu, 808 nm-triggered optical thermometry based on up-conversion luminescence of Nd^{3+}/Yb^{3+}/Er^{3+} doped MIn_2O_4 (M = Ca, Sr and Ba) phosphors, Dalton Trans. 10 (2018) 1039, https://doi.org/10.1039/C8DT00913A.

[11] I.E. Kolesnikov, E.V. Golyeva, A.A. Kalinichev, M.A. Kurochkin, E. Landeranta, M. D. Mikhailov, Nd^{3+} single doped YVO_4 nanoparticles for sub-tissue heating and thermal sensing in the second biological window, Sensor. Actuator. B Chem. 243 (2017) 338–345, https://doi.org/10.1016/j.snb.2016.12.005.

[12] K.C. Liu, Z.Y. Zhang, C.X. Shan, Z.Q. Feng, J.S. Li, C.L. Song, Y.N. Bao, X.H. Qi, B. Dong, A flexible and superhydrophobic upconversion-luminescence membrane as an ultrasensitive fluorescence sensor for single droplet detection, Light Sci. Appl. 5 (2016), e16136, https://doi.org/10.1038/lsa.2016.136.

[13] X. Zhang, R. Gao, Z. Wang, Y. Zhang, Y. Hu, L. Sun, F. Fu, X. Ai, J.P. Zhang, Effect of excitation mode on the upconversion luminescence of β-$NaYF_4$: Yb/Er nanocrystals, Chem. Phys. Lett. 779 (2021), 138880, https://doi.org/10.1016/j.cplett.2021.138880.

[14] Z. Yu, Z. Xia, E. Liu, Q. Liu, Synthesis, up-conversion luminescence and thermometry of Yb^{3+}/Er^{3+} co-doped $La_{2.4}Mo_{1.6}O_8$ phosphors, Dalton Trans. 45 (2016) 16240–16245, https://doi.org/10.1039/C6DT03059A.

[15] P. Liu, J. Liu, Y. Zhang, Z. Xia, Y. Xu, Morphology controlled synthesis of $Ba_4Bi_3F_{17}$: Er^{3+}, Yb^{3+} and the dual-functional temperature sensing and optical heating applications, J. Alloys Compd. 844 (2020), 156116, https://doi.org/10.1016/j.jallcom.2020.156116.

[16] J. Zhang, Z. Hao, J. Li, X. Zhang, Y. Luo, G. Pan, Observation of efficient population of the red-emitting state from the green state by non-multiphonon relaxation in the Er^{3+}-Yb^{3+} system, Light Sci. Appl. 4 (2015) e239, https://doi.org/10.1038/lsa.2015.12.

[17] Q. Zhan, J. Qian, H. Liang, G. Somesfalean, D. Wang, S. He, Z. Zhang, S. Andersson-Engels, Using 915 nm laser excited $Tm^{3+}/Er^{3+}/Ho^{3+}$-doped $NaYbF_4$ upconversion nanoparticles for in vitro and deeper in vivo bioimaging without overheating irradiation, ACS Nano 5 (2011) 3744–3757, https://doi.org/10.1021/nn200110j.

[18] X. Xie, X. Liu, Upconversion goes broadband, Nat. Mater. 11 (2012) 842–843, https://doi.org/10.1038/nmat3426.

[19] Y. Ji, W. Xu, N. Ding, H. Yang, H. Song, Q. Liu, H. Agren, J. Widengren, H. Liu, Huge upconversion luminescence enhancement by a cascade optical field modulation strategy facilitating selective multispectral narrow-band near-infrared photodetection, Light Sci. Appl. 9 (2020) 1–12, https://doi.org/10.1038/s41377-020-00418-0.

[20] H. Suo, F. Hu, X. Zhao, Z. Zhang, T. Li, C. Duan, M. Yin, C. Guo, All-in-one thermometer-heater up-converting platform YF_3: Yb^{3+}, Tm^{3+} operating in the first biological window, J. Mater. Chem. C 5 (2017) 1501–1507, https://doi.org/10.1039/C6TC05449H.

[21] K. Shou, C. Qu, Y. Sun, H. Chen, S. Chen, L. Zhang, H. Xu, X. Hong, A. Yu, Z. Cheng, Multifunctional biomedical imaging in physiological and pathological conditions using a NIR-II probe, Adv. Funct. Mater. 27 (2017), 1700995, https://doi.org/10.1002/adfm.201700995.

[22] W. Xu, Y. Hu, L. Zheng, Z. Zhang, W. Cao, H. Liu, X. Wu, Enhanced NIR-NIR luminescence from $CaWO_4$: Nd^{3+}/Yb^{3+} phosphors by Li^+ codoping for thermometry and optical heating, J. Lumin. 208 (2019) 415–423, https://doi.org/10.1016/j.jlumin.2019.01.005.

[23] Z. Wang, P. Zhang, Q. Yuan, X. Xu, P. Lei, X. Liu, L. Dong, J. Feng, H. Zhang, Nd^{3+}-sensitized $NaLuF_4$ luminescent nanoparticles for multimodal imaging and temperature sensing under 808 nm excitation, Nanoscale 7 (2015) 17861–17870, https://doi.org/10.1039/C5NR04889C.

[24] B. Cao, Y. Bao, Y. Liu, J. Shang, Z. Zhang, Y. He, Z. Feng, B. Dong, Wide-range and highly-sensitive optical thermometers based on the temperature-dependent energy transfer from Er to Nd in Er/Yb/Nd codoped $NaYF_4$ upconversion nanocrystals, Chem. Eng. J. 385 (2020), 123906, https://doi.org/10.1016/j.cej.2019.123906.

[25] K.C. Camargo, R.R. Pereira, L.D. Santos, S.D. Oliveira, R.R. Goncalves, L. Menezes, Continuous wave near-infrared phonon-assisted upconversion in single Nd^{3+}-doped yttria nanoparticles, J. Lumin. 192 (2017) 963–968, https://doi.org/10.1016/j.jlumin.2017.08.031.

[26] Z. Nie, X. Ke, D. Li, Y. Zhao, L. Zhu, R. Qiao, X.L. Zhang, $NaYF_4$: Yb, Er, Nd@ $NaYF_4$: Nd upconversion nanocrystals capped with Mn: TiO_2 for 808 nm NIR-triggered photocatalytic applications, J. Phys. Chem. C 123 (2019) 22959–22970, https://doi.org/10.1021/acs.jpcc.9b05234.

[27] G. Xiang, M. Yang, Z. Liu, Y. Wang, S. Jiang, L. Li, X. Zhou, L. Ma, X. Wang, J. Zhang, Thermally enhanced near-infrared luminescence in $CaSc_2O_4$: Yb^{3+}/Nd^{3+} nanorods for temperature sensing and photothermal conversion, Ceram. Int. 48 (2022) 23436–23443, https://doi.org/10.1016/j.ceramint.2022.04.337.

[28] E.M. Dianov, Bismuth-doped optical fibers: a challenging active medium for near-IR lasers and optical amplifiers, Light Sci. Appl. 1 (2012) e12, https://doi.org/10.1038/lsa.2012.12.

[29] G. Xiang, M. Yang, Z. Liu, Y. Wang, S. Jiang, X. Zhou, L. Li, L. Ma, X. Wang, J. Zhang, Near-Infrared-to-Near-Infrared optical thermometer BaY_2O_4: Yb^{3+}/Nd^{3+} assembled with photothermal conversion performance, Inorg. Chem. 61 (2022) 5425–5432, https://doi.org/10.1021/acs.inorgchem.2c00432.

[30] P. Haro-González, I.R. Martin, L.L. Martin, S.F. Leon-Luis, C. Perez-Rodriguez, V. Lavin, Characterization of Er^{3+} and Nd^{3+} doped Strontium Barium Niobate glass ceramic as temperature sensors, Opt. Mater. 33 (2011) 742–745, https://doi.org/10.1016/j.optmat.2010.11.026.

[31] C. Pérez-Rodríguez, L.L. Martín, S.F. León-Luis, I.R. Martin, K.K. Kiran, C. K. Jayasankar, Relevance of radiative transfer processes on Nd^{3+} doped phosphate glasses for temperature sensing by means of the fluorescence intensity ratio technique, Sensor. Actuator. B Chem. 195 (2014) 324–331, https://doi.org/10.1016/j.snb.2014.01.037.

[32] W. Xu, Q. Song, L. Zheng, Z. Zhang, W. Cao, Optical temperature sensing based on the near-infrared emissions from Nd^{3+}/Yb^{3+} codoped $CaWO_4$, Opt. Lett. 39 (2014) 4635–4638, https://doi.org/10.1364/OL.39.004635.

[33] P. Huang, W. Zheng, D. Tu, X. Shang, M. Zhang, R. Li, J. Xu, Y. Liu, X. Chen, Unraveling the electronic structures of neodymium in $LiLuF_4$ nanocrystals for ratiometric temperature sensing, Adv. Sci. 6 (2019), 1802282, https://doi.org/10.1002/advs.201802282.

[34] J.X. Meng, F.J. Zhang, W.F. Peng, W.J. Wan, Q.L. Xiao, Q.Q. Chen, L.W. Cao, Z. L. Wang, Fluorescence properties of novel near-infrared phosphor $CaSc_2O_4$: Ce^{3+}, Nd^{3+}, J. Alloys Compd. 508 (2010) 222–225, https://doi.org/10.1016/j.jallcom.2010.08.064.

[35] G. Xiang, M. Yang, Q. Xia, S. Jiang, Y. Wang, X. Zhou, L. Li, L. Ma, X. Wang, J. Zhang, Ultrasensitive optical thermometer based on abnormal thermal quenching Stark transitions operating beyond 1500 nm, J. Am. Ceram. Soc. 104 (2021) 5784–5793, https://doi.org/10.1111/jace.17981.

[36] G. Gao, D. Busko, S. Kauffmann-Weiss, A. Turshatov, I.A. Howard, B.S. Richards, Wide-range non-contact fluorescenceintensity ratio thermometer based on Yb^{3+}/Nd^{3+} co-doped La_2O_3 microcrystals operating from 290 to 1230 K, J. Mater. Chem. C 6 (2018) 4163–4170, https://doi.org/10.1039/C8TC00782A.

[37] S. Jiang, P. Zeng, L. Liao, S. Tian, H. Guo, Y. Chen, C. Duan, M. Yin, Optical thermometry based on upconverted luminescencein transparent glass ceramics containing $NaYF_4$: Yb^{3+}/Er^{3+} nanocrystals, J. Alloys Compd. 617 (2014) 538–541, https://doi.org/10.1016/j.jallcom.2014.08.080.

[38] I.E. Kolesnikov, D.V. Mamonova, A.A. Kalinichev, M.A. Kurochkin, V.A. Medvedev, E.Y. Kolesnikov, E. Lähderanta, A.A. Manshina, Constructing of efficient dual activating ratiometricYVO_4: Nd^{3+}/Eu^{3+} nanothermometer: co-doping or mixture, Nanoscale 12 (2020) 5953–5960, https://doi.org/10.1039/C9NR08358H.

[39] G. Xiang, Q. Xia, X. Liu, X. Wang, Optical thermometrybased on the thermally coupled energy levels of Er^{3+} in upconversionmaterials, Dalton Trans. 49 (2020), 17115, https://doi.org/10.1039/D0DT03100C.

[40] S.A. Wade, S.F. Collins, G.W. Baxter, Fluorescence intensityratio technique for optical fiber point temperature sensing, J. Appl. Phys. 94 (2003) 4743–4756, https://doi.org/10.1063/1.1606526.

[41] K. He, Y. Shen, Q. Yang, G. Bai, S. Xu, L. Chen, Thermally enhanced anti-Stokes emission of Yb/Nd codoped lithium niobate ceramics for temperature sensing, Opt. Mater. 112 (2021), 110724, https://doi.org/10.1016/j.optmat.2020.110724.

[42] X.F. Wang, Y.M. Wang, Y.Y. Bu, X.H. Yan, J. Wang, P.Q. Cai, V. Thiquynh, J.S. Hyo, Influence of doping and excitation powers on optical thermometry in Yb^{3+}-Er^{3+} doped $CaWO_4$, Sci. Rep. 7 (2017), 43383, https://doi.org/10.1038/srep43383.

[43] A. Benayas, R.B. Del, A. Pérez-Delgado, K. Santacruz-Gomea, D. Jaque, G.A. Hirata, F. Vetrone, Nd: YAG near-infrared luminescent nanothermometers, Adv. Opt. Mater. 3 (2015) 687–694, https://doi.org/10.1002/adom.201400484.

[44] U. Rocha, J. Silva, W.F. Silva, I. Guedes, A. Benayas, L.M. Maestro, M.A. Elias, E. Bovero, F. Veggel, J. Sole, D. Jaque, Subtissue thermal sensing based on neodymium-doped LaF_3 nanoparticles, ACS Nano 7 (2013) 1188–1199, https://doi.org/10.1021/nn304373q.

[45] M. Quintanilla, Y. Zhang, L.M. Liz-Marzán, Subtissue plasmonic heating monitored with CaF_2: Nd^{3+}, Y^{3+} nanothermometers in the second biological window, Chem. Mater. 30 (2018) 2819–2828, https://doi.org/10.1021/acs.chemmater.8b00806.

[46] D. Wawrzynczyk, A. Bednarkiewicz, M. Nyk, W. Strek, M. Samoc, Neodymium (III) doped fluoride nanoparticles as non-contact optical temperature sensors, Nanoscale 4 (2012) 6959–6961, https://doi.org/10.1039/C2NR32203J.

[47] G. Dantelle, M. Matulionyte, D. Testemale, A. Cantarano, F. Vetrone, Nd^{3+} doped $Gd_3Sc_2Al_3O_{12}$ nanoparticles: towards efficient nanoprobes for temperature sensing, Phys. Chem. Chem. Phys. 21 (2019) 11132–11141, https://doi.org/10.1039/C9CP01808E.

[48] L. Marciniak, A. Bednarkiewicz, D. Hreniak, W. Strek, The influence of Nd^{3+} concentration and alkali ions on the sensitivity of non-contact temperature measurements in $ALaP_4O_{12}$: Nd^{3+} (A= Li, K, Na, Rb) nanocrystalline luminescent thermometers, J. Mater. Chem. C 4 (2016) 11284–11290, https://doi.org/10.1039/C6TC03396B.

[49] I.E. Kolesnikov, A.A. Kalinichev, M.A. Kurochkin, E.V. Golyeva, E. Yu Kolesnikov, A.V. Kurochkin, E. Lahderanta, M.D. Mikhailov, YVO_4: Nd^{3+} nanophosphors as NIR-to-NIR thermal sensors in wide temperature range, Sci. Rep. 7 (2017), 18002, https://doi.org/10.1038/s41598-017-18295-w.

[50] X. Zhou, Y.J. Wang, H.W. Wang, L. Xiang, Y.L. Yan, L. Li, G.T. Xiang, Y.H. Li, S. Jiang, X. Tang, X.J. Zhou, Nd^{3+} and Nd^{3+}/Yb^{3+}-incorporated complexes as optical thermometer working in the second biological window, Sens. Biosensing Res. 29 (2020), 100345, https://doi.org/10.1016/j.sbsr.2020.100345.

[51] X. Zhou, R. Wang, G. Xiang, S. Jiang, L. Li, X. Luo, Y. Pang, Y. Tian, Multi-parametric thermal sensing based on NIR emission of Ho (III) doped $CaWO_4$ phosphors, Opt. Mater. 66 (2017) 12–16, https://doi.org/10.1016/j.optmat.2017.01.035.